Principle of the electrically induced Transient Current Technique

Jinst

Published by IOP Publishing for Sissa Medialab

Received: *February 14, 2018*
Revised: *March 26, 2018*
Accepted: *April 20, 2018*
Published: *May 18, 2018*

Principle of the electrically induced Transient Current Technique

J. Bronuzzi,[a,b,1] **M. Moll,**[a] **D. Bouvet,**[c] **A. Mapelli**[a] **and J.M. Sallese**[b]

[a] *Experimental Physics Department, European Organization for Nuclear Research (CERN), Route de Meyrin 385, Meyrin, 1217 Switzerland*
[b] *Group of Electronics Device Modeling and Technology, École Polytechnique Fédérale de Lausanne (EPFL), Route Cantonale, Lausanne, 1015 Switzerland*
[c] *Center of Micronanotechnology, École Polytechnique Fédérale de Lausanne (EPFL), Route Cantonale, Lausanne, 1015 Switzerland*

E-mail: jacopo.bronuzzi@cern.ch

Abstract: In the field of detector development for High Energy Physics, the so-called Transient Current Technique (TCT) is used to characterize the electric field profile and the charge trapping inside silicon radiation detectors where particles or photons create electron-hole pairs in the bulk of a semiconductor device, as PiN diodes. In the standard approach, the TCT signal originates from the free carriers generated close to the surface of a silicon detector, by short pulses of light or by alpha particles. This work proposes a new principle of charge injection by means of lateral PN junctions implemented in one of the detector electrodes, called the electrical TCT (el-TCT). This technique is fully compatible with CMOS technology and therefore opens new perspectives for assessment of radiation detectors performances.

Keywords: Detector modelling and simulations II (electric fields, charge transport, multiplication and induction, pulse formation, electron emission, etc); Radiation damage to detector materials (solid state); Radiation damage to electronic components; Solid state detectors

[1]Corresponding author.

https://doi.org/10.1088/1748-0221/13/05/P05021

2018 JINST 13 P05021

Contents

1 Introduction

The Transient Current Technique (TCT) is based on the measurement of the current pulse shape produced by free charge carriers drifting within the electric field of a depleted semiconductor region [1]–[5]. TCT is typically applied to characterize silicon PiN diodes for particle or light detection, i.e. PN junction devices with a thin strongly doped region acting as electrode and a wide lightly doped region used to build up a depleted volume serving to detect the particles or photons by ionization (see figure 1). TCT allows the inspection of the electric field profile inside the diode bulk. This is possible by analysing the waveform of the transient current induced by drifting free charges. Since the electric field profile depends on the local space charge density, TCT can be exploited to evaluate the presence of fixed charges originating from ionized dopants or traps. The latter being for example the main reason for the radiation induced performance degradation of silicon particle detectors in high luminosity hadron colliders [2, 6, 7]. The sensing region of a typical high energy particle detector architecture is sketched in figure 1. In the transient current technique, electron-hole pairs are generated in silicon by means of a short laser pulse with a wavelength from the IR to the visible range, i.e. 1064 nm to 404 nm, (as is the case in figure 1) of some tens of ps [8]. Alpha particles can also be used for charge injection [9]. Illuminating the P+ electrode side and using a wavelength that is absorbed in the first few microns of the silicon as depicted in figure 1 (e.g. λ = 660 nm with an absorption coefficient of 2.57×10^3 cm^{-1} [10] and therefore a penetration depth of 3.89 μm), the generated holes are immediately collected by the p-type electrode, while the electrons drift until reaching the ohmic contact after some tens of ns. These drifting charges induce a current

2018 JINST 13 P05021

in electrodes according to the Shockley-Ramo's theorem [11]. In case of a uniformly doped layer the electric field is linear across the device. The movement of an electron cloud, generated close to the P+-contact and drifting towards the N+-contact, and the corresponding transient current is illustrated in figure 1. The shape of the transient current pulse can be used to reconstruct the local electric field inside the depleted region [2, 12]. TCT is therefore a very powerful tool to determine the electric field profiles (i.e. the space charge profile) and the carrier lifetimes. Moving the laser over the detector surface allows to establish the corresponding 2D profiles, provided the device is accessible to the laser beam.

Illumination with lasers is the standard way of generating the charge carriers used to obtain the transients in TCT. This requires the use of sub-nanosecond pulsed lasers and the implementation of openings in the metal layers of the device under test to allow for light penetration. This "light injection TCT" is therefore usually performed on dedicated TCT test structures.

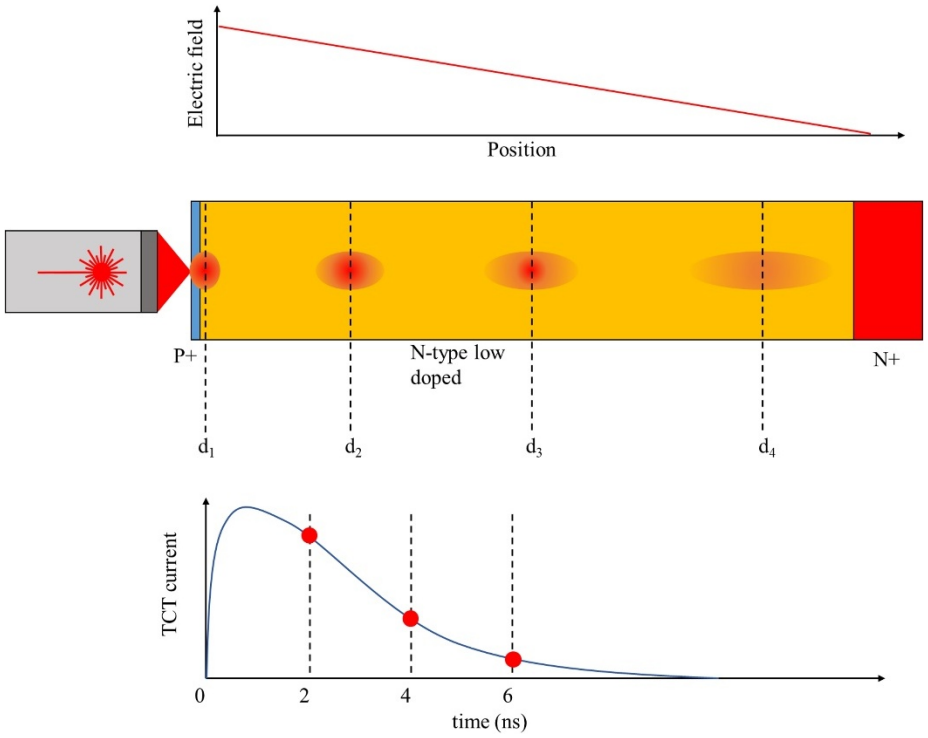

Figure 1. Principle of light injection TCT. Electrons are generated inside the bulk of a reverse biased diode using a pulsed laser beam. These drift along the diode and generate a transient current whose shape is related to the profile of the electric field. In this figure, the positions d_i refer to the positions inside the diode, considering that at time 0 ns the cloud is located at position d_1.

In this article, a different approach, called electrical injection TCT (el-TCT), is discussed. It is obtained through the implementation of a lateral PiN structure in an operational device, that is assumed to give only little or no impact on its performance and would allow to apply the TCT technique during irradiation tests and experiments. Such characterization is impossible to perform with light injection TCT. In the present work we provide a proof of concept for el-TCT while the implementation of el-TCT structures in operating devices is not studied in detail. This article contains a preliminary study of the concept of el-TCT, that is evaluated through numerical

2018 JINST 13 P05021

simulations carried out with the Sentaurus TCAD software package [13], resulting in an adaptation of the silicon diode layout for el-TCT applications. These simulations are followed by the design, fabrication and experimental characterisation of optimized silicon structures. The experimental data presented in this paper allows a preliminary assessment of el-TCT with respect to the standard light injection TCT.

2 Principle and simulations of electrical injection TCT

2.1 The device architecture

A cross section of the el-TCT device structure is shown in figure 2a. and table 1 summarises the device parameters used for the TCAD simulations. The n-type substrate doping concentration was set to $7 \times 10^{11}\,\mathrm{cm}^{-3}$. Gaussian doping profiles with maximum concentrations at the surface have been used to simulate the strongly doped silicon regions generated by implantation and then diffusion. The doping of the top side extends into the P_W and N_W regions, that are the p-type (P+) and n-type strongly (N+) doped region on the front side of the device (see figure 2a). In the S regions (corresponding to the spaces between the P_W and the N_W regions), the doping is obtained by lateral diffusion from the P_W and the N_W regions. The thickness Th of the device is 320 µm. The simulated structure represents only a small part of the devices produced in this work (see figure 8). In the el-TCT concept, injection of free charge carriers (electrons in our case) is done by means of n-type implants surrounded by p-type doped regions (respectively red and blue regions in figure 2). Note that the p-type doped layers constitute the front electrodes of the detector which are also implemented in devices for optical TCT, while the n-type doped layers are specific to el-TCT architectures. The electrons are injected into the lightly doped substrate by pulsing node B from $V_{bias,B}$ to $V_{trans,B}$ (e.g. for 1 ns), while the voltage difference between nodes A and C is set to operate the PN junction in reverse bias (i.e. $V_{bias,A} - V_{bias,C} < 0$) creating an electric field in the bulk of the PiN structure. A biasing scheme (including the voltage waveform applied to contact B) is shown in figure 2b. This architecture and the related biasing sequence are optimized so that injection takes place at node B. The principle of operation and device optimization will be addressed in the next section.

Table 1. List of doping parameters for TCAD simulation. P_W, N_W, S, Th, DL_p, DL_n, DL_n are expressed in µm and C_p, $C_{B,n}$, $C_{C,n}$ are expressed in cm^{-3}. C_p is the peak P-type doping concentration at surface, $C_{B,n}$ is the peak N-type doping concentration at node B, $C_{C,n}$ is the peak N-type doping concentration at surface (back side, contact C), DL_p is the P-type doping Gaussian width, $DL_{B,n}$ is the N-type doping Gaussian width at node B, $DL_{C,n}$ is the N-type doping Gaussian width (back side, contact C).

P_W	N_W	S	Th	C_p	$C_{A,n}$	$C_{C,n}$	DL_p	$DL_{B,n}$	$DL_{C,n}$
7	3	2	320	4.5×10^{18}	5.82×10^{19}	10^{19}	1.25	1.02	0.7

3 Principle of charge injection

The injection of carriers into the lightly doped region depends strongly on the shape of the doping profiles and the distance S between the peaks of the Gaussian profiles of the implants, i.e. the distance between the edges of the implanted areas (see figure 2 and table 1).

2018 JINST 13 P05021

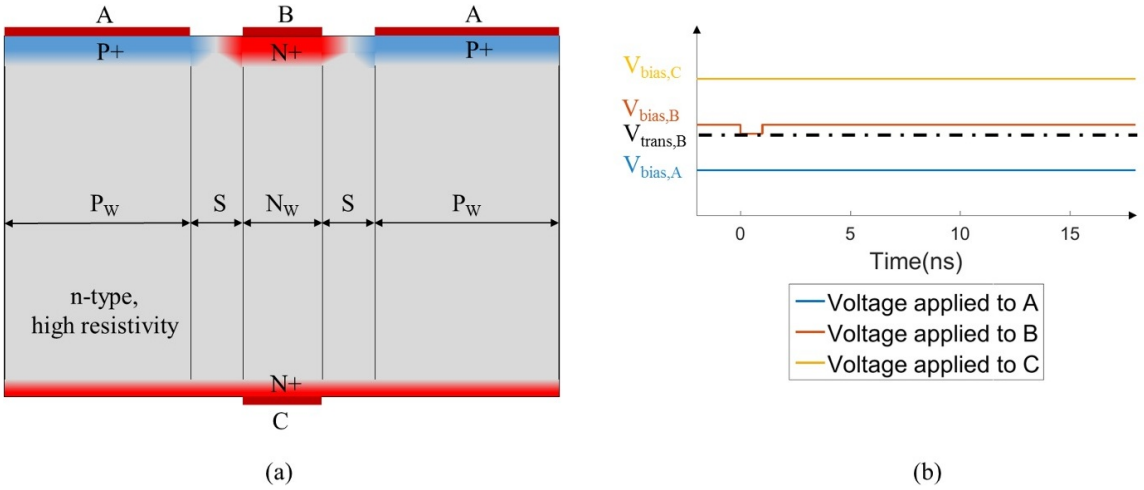

Figure 2. (a) Cross section of a device for el-TCT and (b) scheme of the applied voltage signals for el-TCT. Diffusion doping is shown in the gap between the electrodes. P+ and N+ indicates respectively p-type and n-type doped regions.

A static IV characteristic obtained from TCAD simulations of the current exiting at node C versus the voltage applied at node B (the voltages applied at nodes C and A are respectively +200 V and +0 V) is shown in figure 3. The following physics processes are implemented for the performed Sentaurus TCAD simulations (using the default settings if not mentioned otherwise): high field velocity saturation for electrons and holes, with the low field mobilities equal to 1417 cm^2/Vs for electrons and 470.5 cm^2/Vs for holes, Shockley-Read-Hall recombination (depending on electric field, doping and temperature), Auger recombination and impact ionization for electrons and holes.

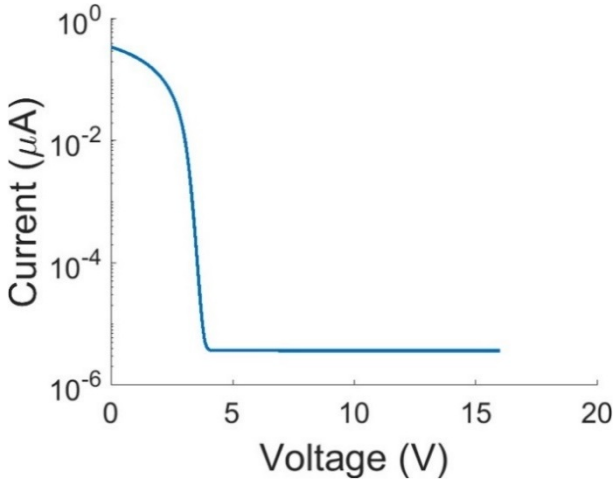

Figure 3. Static IV characteristic of the current at node C versus the positive voltage at node B (voltages applied at node C and A are respectively +200 V and +0 V).

As long as the voltage at node B is higher than +4 V, current does not flow. In other words, applying a voltage between A and C so that the PiN diode remains reverse-biased blocks injection of electrons from B to C. The injection of electrons becomes effective only when the voltage on

2018 JINST 13 P05021

the n-type node B is lower than +4 V. For these voltage values, the IV characteristic follows a resistive behaviour. A current appears between nodes B and C during injection, whereas the lateral PN junction remains reverse-biased and controls the electrostatic potential below the n-type doped region at node B (and therefore the current between nodes A and B). In fact, the injection process is controlled by the fringing electric field created by the lateral p-type and n-type doped layers.

In order to understand how electrical injection is controlled by external voltages, a cross section of the potential profile at the centre of the device is plotted in figure 4 during transient operation for two relevant biasing conditions: (a) with no voltage pulse applied (before 0 ns, with $V_{bias,B}$= +4 V) and (b) with a pulse voltage of $V_{trans,B}$= +3 V. The 2D plot of the conduction band edge energy before the pulse reveals the presence of an energy barrier that blocks electrons to be injected. This barrier is visible in the conduction band edge potential plot of figure 4 obtained along the centre of the device, i.e. along the injecting channel. The voltage applied to that p-type doped layer creates a lateral barrier which encloses and isolates the source of electrons (n-type node). Similarly, the electron density along the same line is shown in figure 4a and it is possible to see that the "channel" ends when the electron density becomes negligible, which corresponds to a depth of about 4 µm.

Next, when the voltage applied at node B is lowered to +3 V during 1 ns, the shape of the potential is modified and a channel starts to open (see figure 4b). Indeed, the energy barrier for electrons is decreased. After 1 ns, the electron concentration at 4 µm is about 3×10^{13} cm^{-3}, much higher than before the pulse (3×10^{10} cm^{-3}).

Finally, when the potential at node B is reset to the off-state potential after 1 ns, the energy barrier goes back to its initial value and the channel switches off again. The time scale of the pulse corresponds to the time needed for electrons to reach the region where the electric field created by the reverse biased PiN junction will make them drift towards node C (corresponding to the blue area in figure 4) preventing electrons to flow towards node B. It is this displacement current that creates the transient current signal at the output node C.

3.1 Thermionic injection

To get a deeper understanding of the electrical injection principle, the influence of biasing voltages is analysed by carrying out TCAD simulations. Six combinations of voltages have been used and are listed in table 2. In all cases, the voltage applied to contact A is equal to 0 V, the voltage applied to node C is equal to +200 V, and the duration of the pulse applied to node B is 1 ns, as shown in figure 2b. The current is always recorded at node C.

As shown in figure 5a and 5b, the current height depends solely on the pulse voltage $V_{trans,B}$, which can be seen by comparing the current signals of combinations 4 and 6. Combination 3 shows no current pulse, as the barrier blocks the electron injection. In case of combination 5, we observe a significant change of the shape of the pulse. This is because the injected charge is high enough to locally modify the electric field of the diode during the drift (see figure 5c, where the Y component of the electric field during the drift is shown when the electron cloud is located at position 150 µm).

A similar result is obtained by comparing the injected charge Q_{in} and the potential barrier height $\Phi_{B,0}$ (considering figure 4, it is defined as the difference between the maximum of the conduction band edge potential and its value at position 0 µm) at time t = 0 ns (i.e. during the voltage pulse) between the combinations as listed in table 3.

2018 JINST 13 P05021

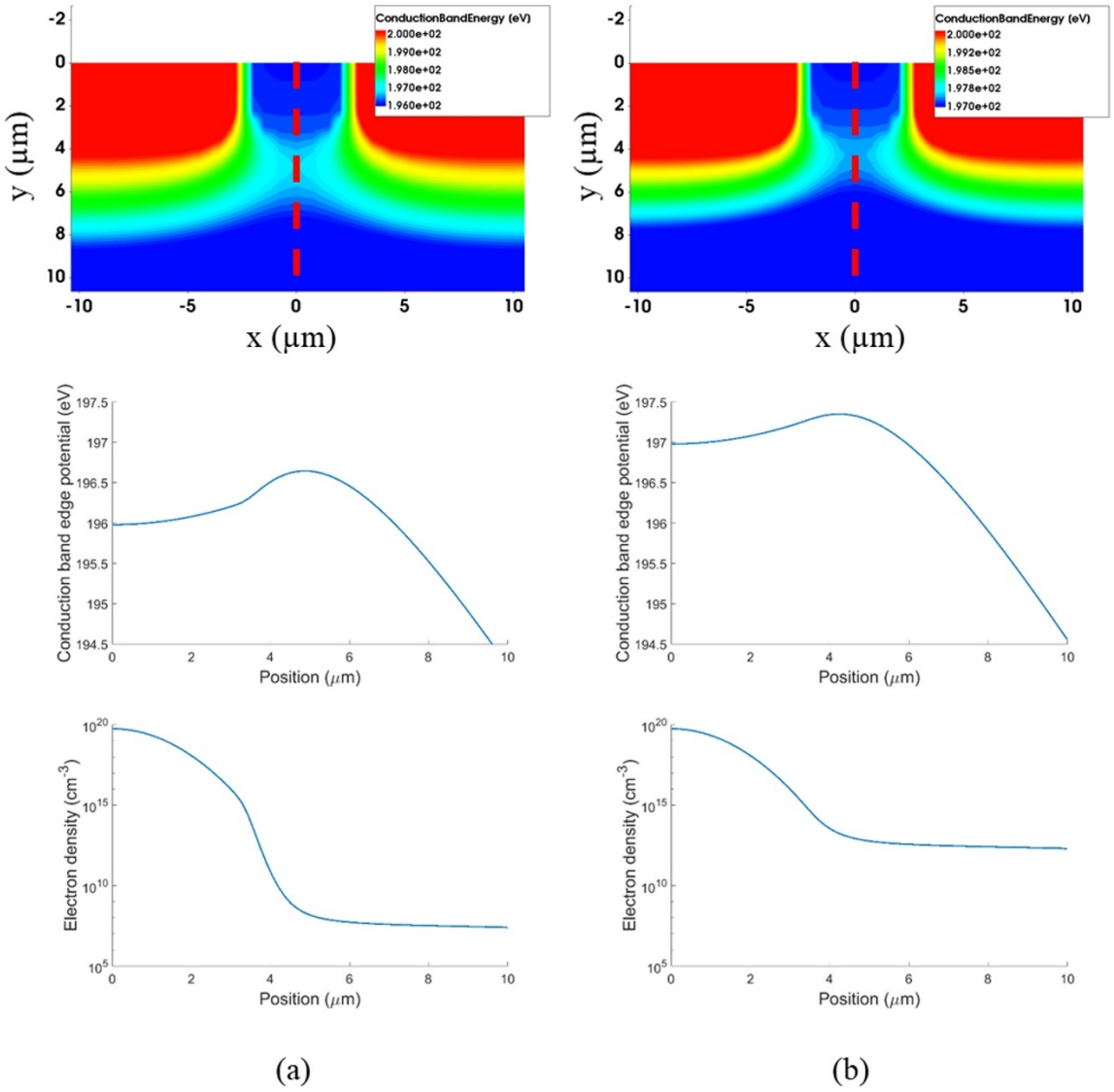

Figure 4. Plots of the conduction band edge potential and injected electron density (a) before the voltage injection pulse and (b) during the pulse. The voltage applied to the p-type doped areas generates a barrier in front of the n-type doped well. When the voltage pulse is applied, the barrier is lowered and electrons can be injected inside the device bulk.

Values reported in table 3 suggest that a higher potential barrier during the voltage pulse leads to a lower density of injected electrons per unit volume, while the height of the barrier before the pulse does not seem to be relevant. It can be assumed that injection of electrons inside the silicon bulk from the n-type doped "injector" occurs mainly through thermionic emission. To show this, a new series of simulations is performed, whose results are showed in figure 6, and then compared with the analytical formula for thermionic emission, in equation (3.1) [14]:

$$J = A^* T^2 e^{\frac{-\phi_B}{kT}} \tag{3.1}$$

where J is the emission current density, k and A^* are the Boltzmann and Richardson constants, T is

2018 JINST 13 P05021

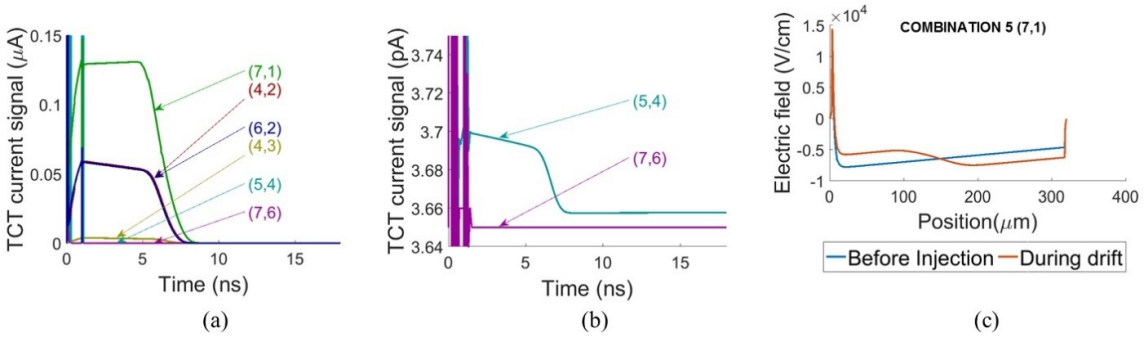

Figure 5. TCT signal currents of the first six combinations, in which the arrows show the combination of positive voltages $V_{bias,B}$ and $V_{trans,B}$, following this notation: ($V_{bias,B}$, $V_{trans,B}$) (a), (b), and Y component of the electric field profile in case of combination 5, before injection and during the drift (c).

Table 2. List of voltage combinations applied at node B in TCAD simulations.

Combination	$V_{bias,B}$ (V)	$V_{trans,B}$ (V)
1	+4	+3
2	+5	+4
3	+7	+6
4	+4	+2
5	+7	+1
6	+6	+2

Table 3. Comparison between injected electrons density and potential barrier height. $\Phi_{B,-t}$ is the potential barrier height before the voltage pulse, $\Phi_{B,0}$ is the Potential barrier height during the pulse, at 0 ns, Q_{in} is the injected charge.

Combination	$\Phi_{B,-t}$ (eV)	$\Phi_{B,0}$ (eV)	Q_{in} (C)
1	0.665	0.371	1.82×10^{-17}
2	1.086	0.665	2.64×10^{-20}
3	2.090	1.568	2.60×10^{-20}
4	0.665	0.315	2.94×10^{-16}
5	2.091	0.306	6.83×10^{-16}
6	1.568	0.315	2.90×10^{-16}

the temperature and Φ_B is the height of the potential barrier. If injection proceeds from thermionic emission, the current densities should scale exponentially with the values of the potential barriers. In figure 6a, it is possible to observe this behaviour. The same is observed for the analytical expression, shown in figure 6a. An important difference between the two curves for the highest value of the potential barrier is observed. In this case, the emission current should be smaller than the reverse bias current value obtained in TCAD simulations, which is the value shown in figure.

2018 JINST 13 P05021

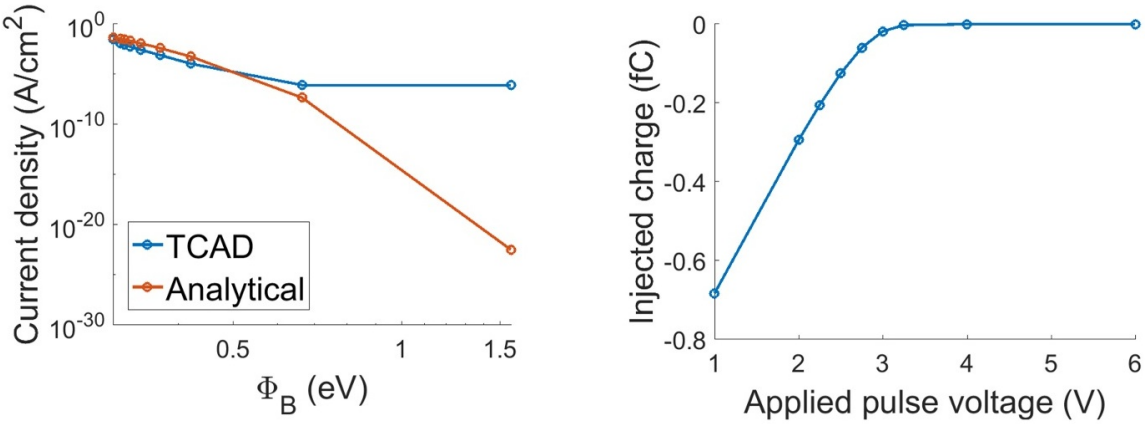

(a) (b)

Figure 6. (a) Comparison between TCAD and the thermionic emission formula of current densities, and (b) injection charge versus applied pulse voltage, i.e. the positive voltage applied to node B during the pulse.

The similar behaviour of the two currents supports the hypothesis that thermionic emission can describe the physical mechanism for charge injection. Figure 6b represents the dependence of the injected charge with respect to the pulse applied at node B (while voltage levels for nodes A and C are kept the same, respectively 0 V and +200 V). Since the barrier height at node B is not proportional to the applied voltage, the dependence of the injected charge density with voltage is not exponential.

3.2 Electrical versus optical excitation

The next step in the study of el-TCT is to perform a qualitative comparison between the TCT signals obtained with light and electrical excitation techniques on a standard diode and an el-TCT device. The physics settings for the TCAD simulations are the same as for the previous study, adding for the light injection the "generation from monochromatic source" at the top of the diode, and "complex refractive index". The optical solver used is Optical Beam [13, pp. 590–591]. Except for the n-type injector implant, the simulated structures share the same technological parameters, therefore, in case of the diode the p-type doping is Gaussian. Concerning the simulation parameters, the voltage difference applied between opposite p-type and n-type doped layers (nodes C and A in figure 2) is fixed to +200 V (positive on node C and 0 V on node A). Other parameters such as the voltage at node B and the parameters of light injection such as the pulse duration, the pulse bias and the intensity of light are listed in table 4. In case of el-TCT device, light is injected from the top, between the contacts A and B, to simulate the masking of the aluminium contacts. The pulse length is 1 ns. Note that these parameters are tuned to obtain concordance between transient current for optical and el-TCT as shown in figure 7, which does not hamper the formal analysis.

According to the numerical simulations, removing the n-type injector does not affect the electric field profile inside the silicon bulk (see figure 7b, where the Y component of the electric field is taken at the centre of the devices), which is a prerequisite to compare both methods. In case of el-TCT, a positive electric field is observed from 0 to 5 µm. This is due to the doping of the n-type

2018 JINST 13 P05021

Table 4. Parameters of simulations of el-TCT and light injection TCT. λ is the laser wavelength, I is the laser intensity, t is the pulse time width, V_{bulk} is the reverse bias voltage.

Electrical injection			Light injection			
$V_{bias,C}$ (V)	$V_{bias,B}$ (V)	$V_{trans,B}$ (V)	λ (nm)	I (mW/cm^2)	t (ps)	V_{bulk} (V)
+200	+4	+3	660	1	50	+200

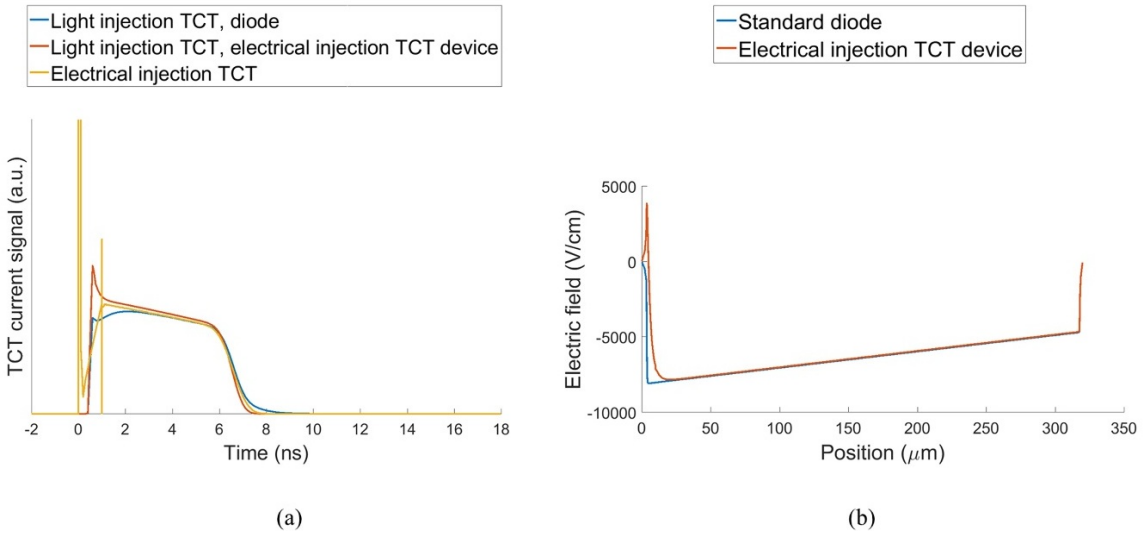

(a) (b)

Figure 7. Comparison between TCAD simulations of light injection TCT and el-TCT. The left plot (a) shows a comparison between light injection TCT on a standard diode and on a device for el-TCT, and electrical injection on an el-TCT device. The right plot (b) shows the profile of the Y component of the electric field at the centre of a standard diode compared to the one at the centre of an el-TCT device.

implant, and does not cause any hole accumulation since holes quickly recombine due to the high n-type doping of the injector. Similarly, the transient currents (see figure 7a) reveal that electrical and light injection TCT are consistent, providing evidence that the concept of el-TCT is meaningful. It is possible to observe peaks in case of light injection between 0 and 2 ns. They are due to the fact that holes are also generated and immediately collected in case of light injection. For electrical injection, only electrons are injected. Moreover, the curve corresponding to the light injection in the diode is smaller than the others between 0 and 2 ns. This is due to the Gaussian profile of the p-type doped silicon, which generates a slow increase of the electric field before the PN junction.

4 Devices and experimental characterization

4.1 Devices and measurement setup

Based on numerical simulations, a device was designed and fabricated at the Center of Micro-nanotechnology at EPFL (CMi), to demonstrate the proof of concept. The device consists of a matrix of n-type doped wells surrounded by a p-type doped silicon, which represent respectively contacts A and B in figure 2. The substrate is a 4-inch n-type silicon wafer and constitutes the "i" region of the PiN diode. In order to achieve a large depletion region, the silicon wafer has a

2018 JINST 13 P05021

nominal resistivity greater than 5000 $\Omega \cdot$ cm, which corresponds to a doping concentration smaller than $10^{12}\,\mathrm{cm}^{-3}$ (similar to the one used in TCAD simulations). The fabrication process flow is summarized in the following lines while more details are given in appendix A. The front side of a silicon wafer is initially implanted with boron (dose $10^{15}\,\mathrm{cm}^{-2}$ and energy 30 keV) through a photoresist mask in order to define the p-type doped regions. Next, an n-type phosphorus implant (dose $10^{16}\,\mathrm{cm}^{-2}$ and energy 30 keV) defines the "injectors" wells through an SiO_2 hard mask. The back side is doped by diffusion of phosphorus (in a POCl3 atmosphere during 15 min at 1100°C). All contacts are obtained by structuring sputtered aluminium. At the end of the process, spreading resistance profiling (SRP) [15] measurements are performed, showing a bulk doping concentration of $3 \times 10^{12}\,\mathrm{cm}^{-3}$. This difference from the nominal resistivity value before processing could be due to high temperature steps during the processing that can e.g. lead to thermal donor generation [16]. Figure 8 shows the top view and cross section of the designed diodes (figure 8a) as well as an optical microscope picture of the top of the fabricated devices (figure 8b).

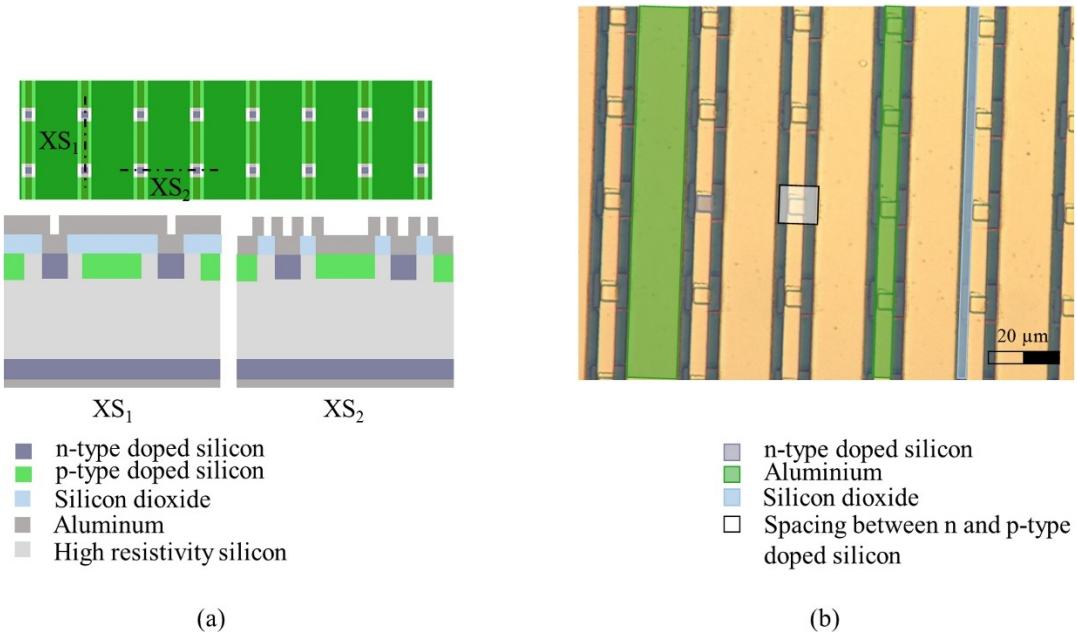

Figure 8. (a) Top view of the layout and cross sections in the vertical (XS_1) and horizontal (XS_2) directions and (b) optical microscope picture of the fabricated device top side.

The circuit used for the el-TCT measurements is shown in figure 9. Concerning the device, the Bulk contact represents the contact to the strongly doped n-type back implant, the n-type contact represents the n-type doped well and the p-type contact represents the p-type doped silicon. The signal generator Picosecond Pulse Labs (model 10,050A) is used as pulse generator. The DC bias is delivered through a bias-tee (Picosecond Pulse Labs model 5531) also used to send the transient current signal to the oscilloscope Agilent DSO9254A (from the Bulk contact). The voltage generator (Keithley 2410) is used to supply the DC high voltage. Attenuators and a signal inverting transformer (Phillips Scientific model 460) are used to shape the signal. The input voltage offset is controlled by using a voltage generator (Agilent E3631A) connected to the signal, before the connection to the n-type contact, through a bias-tee (Mini-Circuits ZFBT-6GW).

2018 JINST 13 P05021

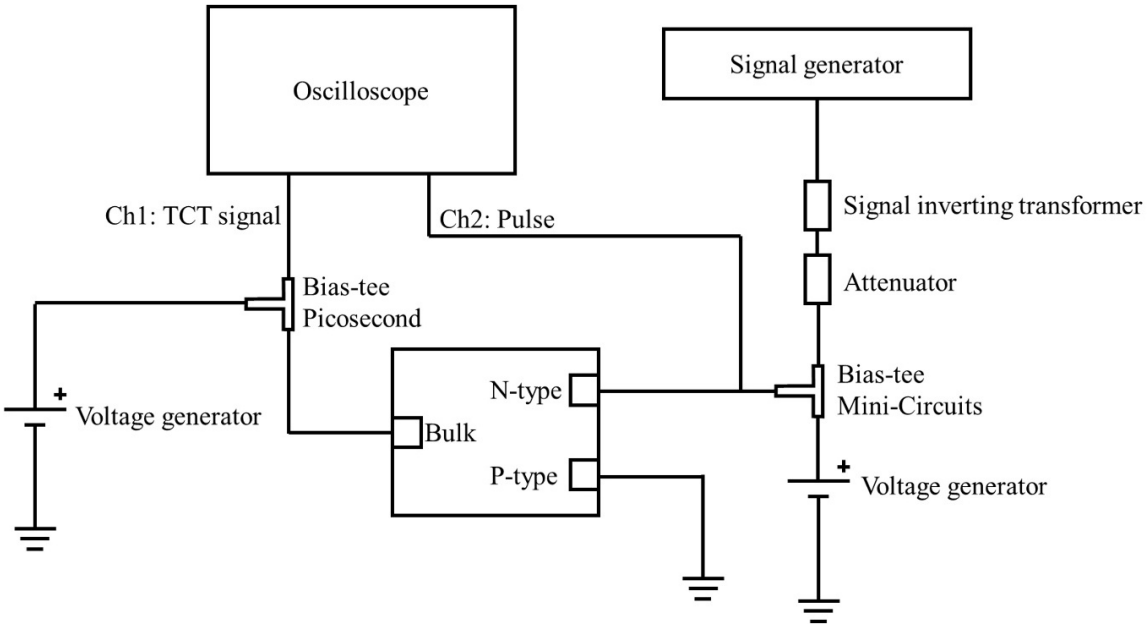

Figure 9. Schematic of the circuit used for the measurement.

In case of light injection, a 50 ps pulse laser (wavelength 660 nm), with a spot diameter of 10 µm positioned in the middle of the device (i.e. shining in the centre of the n-type wells matrix shown in figure 8b). The n-type contact is biased at a value close to the offset voltage used for electrical injection (+4.1 V), and the TCT signal is amplified using the CIVIDEC C2HV Broadband Amplifier (gain 40 dB, bandwidth 2 GHz), connected on the back side of the device. The measured capacitance of the device is 3.54 pF at 100 V, 3.04 pF at 120 V and 2.64 pF at 140 V.

5 Transient current measurements and analysis

The electrical pulse which is applied to the n-type doped well (node B in figure 2) is shown in figure 10a. The overall pulse duration is about 1 ns during which the voltage changes abruptly from +3.75 V to +0.2 V. The transient current generated by the drift of the injected carriers is shown in figure 10b for different back side voltages. It is possible to observe a small distortion at 12 ns. This is due to a parasitic signal inside the circuit for voltage pulse generation, since it is possible to observe the same feature on the injection pulse in figure 10a. Another parasitic pulse is observed at 25 ns, which however is out of the time window of interest for the TCT measurement in figure 10b. Increasing the voltage between nodes A and C (V_{AC}) modifies the shape of the transient current. Up to 2 ns after the electrical pulse, the current increases. This could be due to the increase in the electric field in the lightly doped region, as observed in the TCAD simulations of optical TCT on standard diode in figure 7b, but also due to the finite rise time of the read-out circuit. After 10 ns, it is possible to observe a signal that fades, since the device is not fully depleted.

In order to compare el-TCT with light induced TCT, the normalized transient currents obtained from both methods are shown in figure 10b (V_{AC} are listed in the legend for different measurements), where the reverse PiN diode biases are kept the same for optical and electrical injection methods.

2018 JINST 13 P05021

The normalization has been performed by introducing a constant N (the same for all measurements), according to equation (5.1).

$$i(t)_{\text{el-TCT}} = N i(t)_{\text{lightinjection}} \ . \tag{5.1}$$

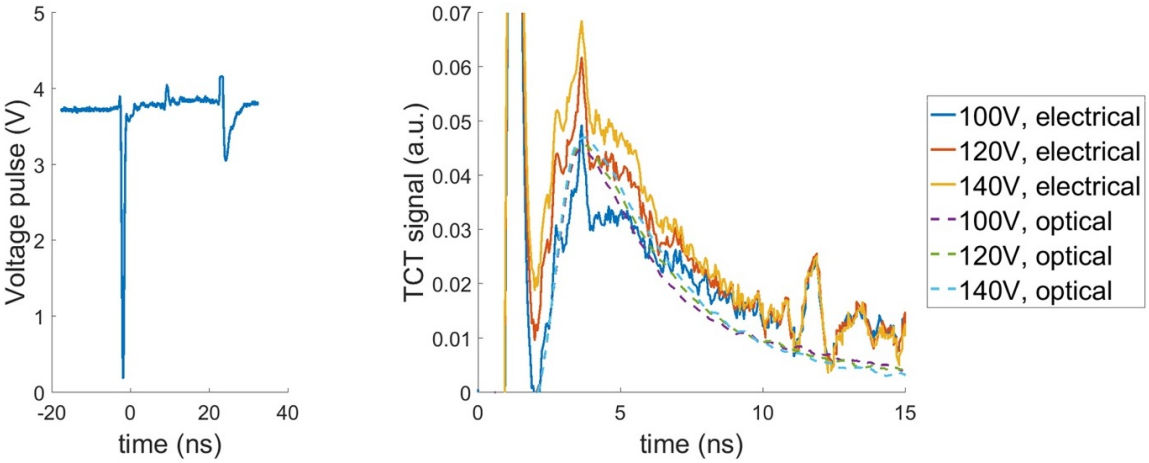

(a) (b)

Figure 10. (a) Voltage pulse applied to the n-type doped wells with positive sign and (b) comparison between TCT signals obtained by light and electrical injection.

Both methods lead to similar shapes of TCT curves (in both cases the time between the rising and decaying of the currents is close to 10 ns), even if the difference between curves obtained from optical TCT is small (a similar behavior observed in TCAD simulations in figure 11b). This confirms that electrical and light injection methods yield equivalent results. The signal-to-noise ratio can be improved by using a dedicated board in which generation of the signal and readout are performed close to the device.

A last validation of the el-TCT comes from TCAD simulations. A modified version of the structure presented in figure 2 (where the parameter S and the bulk doping profile are used as matching parameters, since the doping profile at the end of the fabrication process is different from the nominal one) was used to carry out numerical simulations of el-TCT. The best matching between TCAD and measurements was obtained for a bulk doping of $3 \times 10^{12}\,\text{cm}^{-3}$ (as the one measured with SRP at the end of the process) and an S parameter equal to 0 µm (meaning that in this simulations the regions P_W and N_W are not spaced). A comparison between the simulated and the measured el-TCT signals is presented in figure 11a (see V_{AC} in the legend). An overall agreement with experiments can also be observed for light injection TCT in figure 11b.

This supports the hypothesis that the signal measured after electrical injection can be attributed to the drift of the electrons injected in the low doped silicon. The injected charge can be controlled by the voltage applied to the n-type doped wells and observed as integral of transient current in time-induced charge. This analysis has been carried out both for experimental data and TCAD simulations. The results presented in figure 12 (the value of the peak voltage is the absolute value) reveal a dependence on the $V_{\text{trans,B}}$, similar to the behaviour shown in figure 6b.

2018 JINST 13 P05021

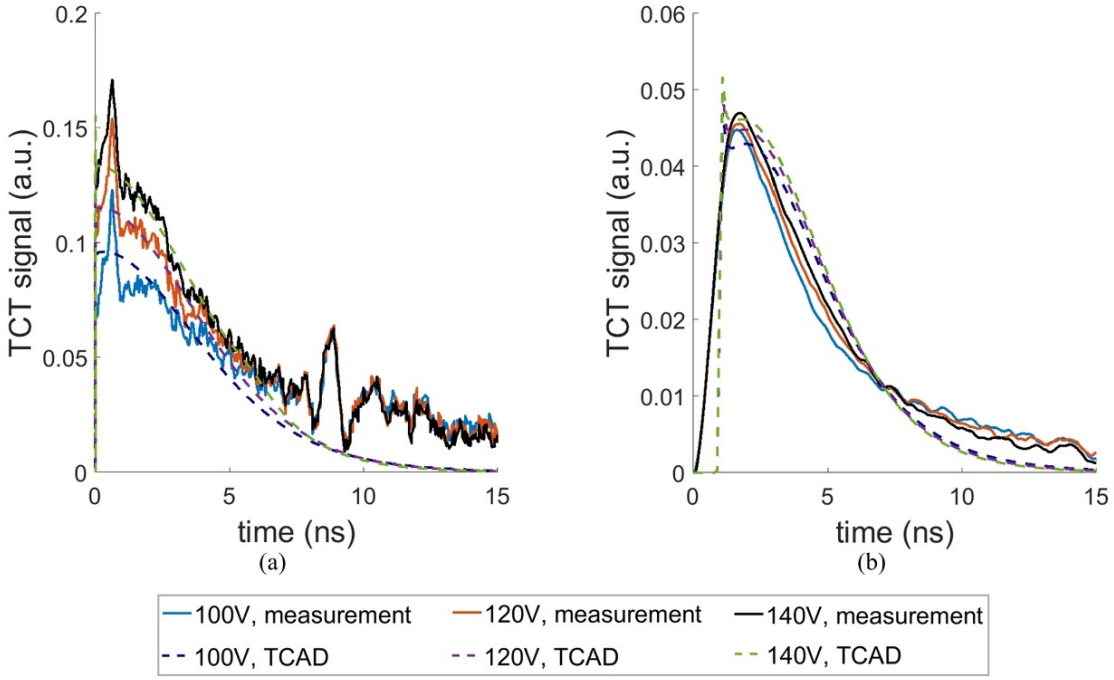

Figure 11. Comparison between TCAD simulations and experimental data of TCT signal obtained by electrical (a) and light (b) injection.

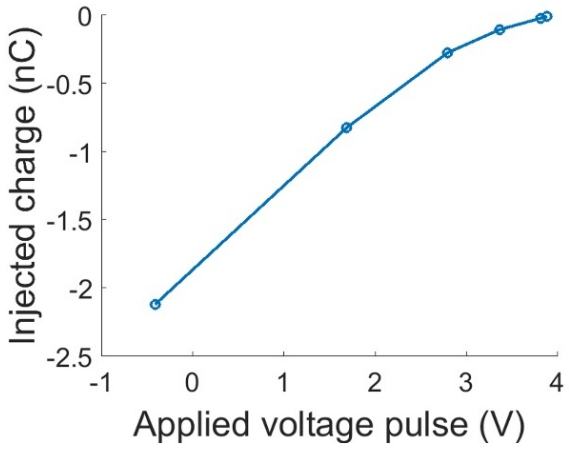

Figure 12. Measured injected charge as a function the voltage applied to node B during the pulse.

6 Conclusion

A new method of carrier injection for TCT characterization, called el-TCT and relying on the concept of electrical charge injection in PiN diodes has been proposed, simulated with TCAD and demonstrated experimentally. The fabricated device structures for el-TCT validated the feasibility to use the electrical charge injection method for device characterization. This new concept allows the integration of a charge injection mechanism into an operational device like e.g. photon or particle detectors. Such modified devices no longer need complex external excitation sources

2018 JINST 13 P05021

(alpha particles, lasers, etc.) to perform TCT. The co-integration of el-TCT with active sensors, where injection and detection can be implemented concurrently, should pave the way to in-situ characterization of solid-state particle or photon detectors.

Acknowledgments

This work was partially performed in the framework of the RD50 collaboration. The authors wish to thank B. Schmidt, E. Sicking and P. Martinengo of CERN for their precious help in the review of this work. The authors are also grateful to the Solid State Detectors team at CERN for their support during the measurements campaign, in particular to J. Gonzalez and M.C. Vignali, to the staff of the CMi cleanroom at EPFL for their help during the fabrication of the devices, and to the reviewer for the precious help for the improvement of the quality of this work.

A Detailed process flow for fabrication of devices for el-TCT

Table 5 summarises the process flow for the fabrication of el-TCT devices. It has been performed at the CMi at the École Polytechnique Fédérale de Lausanne (EPFL). The following machines and services have been used: ACS200 Gen3 for automatic coating and development, Heidelberg VPG200 for direct i-line (355–365 nm) laser writing lithography with 5 mm head, IBS (Ion Beam Service) for ion implantation, Tepla GIGAbatch for photoresist oxygen plasma stripping, Pfeiffer SPIDER600 for sputtering, SPTS APS dielectric etcher for dry etching of SiO2, Disco DAG810 for wafer grinding, Steag Mecapol E460 for chemical mechanical polishing (CMP), Centrotherm furnaces for $POCl_3$ doping, STS multiplex for Al dry etching, Alliance Concept DP650 for Al sputtering.

2018 JINST 13 P05021

Table 5. Process flow for the fabrication of devices for el-TCT.

Step	Process	Parameters
1	Photolithography	Photoresist: AZ ECI 3027, thickness 4 µm
2	Boron ion implantation	Dose 10^{15} cm^{-3}, Energy 30 keV
3	Photoresist stripping	First plasma oxygen, then remover microposit 1165
4	SiO_2 sputtering	Thickness 2 µm
5	Photolithography	Photoresist: AZ ECI 3007, thickness 1.5 µm
6	SiO_2 etching	Reactive ion etching
7	Photoresist stripping	First plasma oxygen, then remover microposit 1165
8	Phosphorus ion implantation	Dose 10^{16} cm^{-3}, Energy 30 keV
9	Photoresist coating	Photoresist: AZ ECI 3027, thickness 4 µm
10	Back side wafer thinning	Grinding and CMP, final thickness 320 µm
11	Photoresist stripping	Remover microposit 1165
12	SiO_2 etching	BHF diluted in water 7:1
13	SiO_2 sputtering	Thickness 2 µm
14	Phosphorus doping	Furnace with $POCl_3$ atmosphere during 15 min at 1100°C
15	SiO_2 etching	BHF diluted in water 7:1
16	SiO_2 sputtering	Thickness 400 nm
17	Photolithography	Photoresist: AZ ECI 3007, thickness 1.5 µm
18	SiO_2 etching	Reactive ion etching
19	Photoresist stripping	First plasma oxygen, then remover microposit 1165
20	Al with 1% of Si sputtering	Thickness 300 nm
21	Photolithography	Photoresist: AZ ECI 3007, thickness 1.5 µm
22	Al with 1% of Si etching	Reactive ion etching
23	Photoresist stripping	First plasma oxygen, then remover microposit 1165
24	Photolithography	Photoresist: AZ ECI 3027, thickness 4 µm
25	Al with 1% of Si sputtering	Thickness 300 nm
26	Photoresist stripping	Remover microposit 1165
27	Dicing	

References

[1] V. Eremin, N. Strokan, E. Verbitskaya and Z. Li, *Development of transient current and charge techniques for the measurement of effective net concentration of ionized charges ($N_{\rm eff}$) in the space charge region of p-n junction detectors*, *Nucl. Instrum. Meth.* **A 372** (1996) 388.

[2] V. Eremin, E. Verbitskaya and Z. Li, *The origin of double peak electric field distribution in heavily irradiated silicon detectors*, *Nucl. Instrum. Meth.* **A 476** (2002) 556.

[3] G. Kramberger et al., *Investigation of Irradiated Silicon Detectors by Edge-TCT*, *IEEE Trans. Nucl. Sci.* **57** (2010) 2294.

[4] M.F. García et al., *High-resolution three-dimensional imaging of a depleted CMOS sensor using an edge Transient Current Technique based on the Two Photon Absorption process (TPA-eTCT)*, *Nucl. Instrum. Meth.* **A 845** (2017) 69.

[5] H. Pernegger et al., *Charge-carrier properties in synthetic single-crystal diamond measured with the transient-current technique*, *J. Appl. Phys.* **97** (2005) 073704.

[6] M. Moll, *Displacement damage in silicon detectors for high energy physics*, *IEEE Trans. Nucl. Sci. 4 April 2018*.

[7] F. Hartmann, *Evolution of Silicon Sensor Technology in Particle Physics*, *Springer Tracts Mod. Phys.* **275** (2017) 1.

[8] J. Härkönen et al., *The Cryogenic Transient Current Technique (C-TCT) measurement setup of CERN RD39 collaboration*, *Nucl. Instrum. Meth.* **A 581** (2007) 347.

[9] H. Pernegger et al., *Charge-carrier properties in synthetic single-crystal diamond measured with the transient-current technique*, *J. Appl. Phys.* **97** (2005) 1.

[10] M.A. Green, *Sol. Energy Materials & Solar Cells Self-consistent optical parameters of intrinsic silicon at* 300 *K including temperature coefficients*, *Sol. Energy Mater. Sol. Cells* **92** (2008) 1305.

[11] S. Ramo, *Currents induced by electron motion*, *Proc. IRE* **27** (1939) 584.

[12] J. Bronuzzi, A. Mapelli, M. Moll and J. Sallese, *Principle and modelling of transient current technique for interface traps characterization in monolithic pixel detectors obtained by CMOS-compatible wafer bonding*, 2016 *JINST* **11** P08016.

[13] Synopsys, *TCAD Sentaurus: Sentaurus Device User Guide*, version I-2013.12 (2013) https://www.synopsys.com/silicon/tcad/device-simulation/sentaurus-device.html.

[14] S.M. Sze, *Measurements of Schottky barrier height*, in *Physics of semiconductor devices*, second edition, Wiley Interscience (1981).

[15] W. Treberspurg, T. Bergauer, M. Dragicevic, J. Hrubec, M. Krammer and M. Valentan, *Measuring doping profiles of silicon detectors with a custom-designed probe station*, 2012 *JINST* **7** P11009.

[16] M. Bruzzi, D. Menichelli, M. Scaringella, J. Härkönen, E. Tuovinen and Z. Li, *Thermal donors formation via isothermal annealing in magnetic Czochralski high resistivity silicon*, *J. Appl. Phys.* **99** (2006) 1.

2018 JINST 13 P05021